The Henryk Niewodniczański
INSTITUTE OF NUCLEAR PHYSICS
ul. Radzikowskiego 152, 31-342 Kraków, Poland

**www.ifj.edu.pl/reports/2000.html**

Kraków, November 2000

---

**Report No 1855/PH**

# FIRST GENERATION OF BOUND OBJECTS IN THE UNIVERSE[1]

S. Stachniewicz and M. Kutschera[1]

[1] also at Institute of Physics, Jagiellonian University, ul. Reymonta 4, 30-059 Kraków, Poland

**Abstract**

We study the formation of first bound objects in the Universe after recombination. We trace the evolution of a spherically symmetric density perturbation in the $\Omega = 1$ Cold Dark Matter (CDM) model with baryon and dark matter contributions respectively $\Omega_b = 0.1$ and $\Omega_{dm} = 0.9$. Physical processes in the collapsing gas relevant to various stages of the nonlinear collapse of low mass objects are considered. We find that the first density perturbations which collapse to form luminous objects have baryon mass in the range $10^3 - 10^4 M_\odot$. The final collapse of these objects is triggered by the cooling due to $H_2$ molecules and it starts early at redshifts $z \sim 20$. The role of the initial baryon overdensity in the collapse of density perturbations in CDM model is studied.

## 1 Introduction

Cosmological observations [1], [2] strongly suggest that the first generation of luminous objects in the Universe could form at high redshifts, possibly as high as $z \sim 10 - 30$ [3]. These first baryonic objects usually are referred to as Population III stars. The formation of first Population III objects ended "dark ages" [4] in the evolution of the Universe. In most popular cosmological models with hierarchical structure formation, the first baryonic objects form from a few $\sigma$ ($\sim 3\sigma$) density fluctuations on small scales that collapse first [5].

[1]This research is partially supported by the Polish State Committee for Scientific Research (KBN), grant no. 2 P03B 112 17.

To study the structure formation powerful 3-dimensional simulations techniques are now available (e.g. [6]). However, much simpler 1-dimensional calculations are sufficient to assess the role of gas dynamical processes which influence crucially the dynamics of collapse of low-mass gas clouds. In this approach the formation of the first cosmological bound objects was studied recently by Haiman, Thoul and Loeb [5] who included in the hydrodynamical simulations detailed thermal and non-equilibrium chemical evolution of the primordial gas. They found that objects of mass lower than linear-theory Jeans mass can form at redshifts $z > 10$. A similar analysis was performed by Tegmark et al. [7] who considered the problem how small were the first cosmological objects.

In this paper we consider the evolution of a single spherically symmetric density perturbation in the early Universe starting soon after recombination until it finally forms a bound stationary object. As an underlying cosmology we choose the $\Omega = 1$ Cold Dark Matter model with $\Omega_b = 0.1$ and $\Omega_{dm} = 0.9$. Our aim here is to extend the analysis of Ref.[5] to study how some assumptions concerning the initial perturbations made in Ref.[5] affect conclusions regarding the cosmological formation of low-mass objects. In particular, we study the sensitivity of the collapse of first clouds to the initial value of the baryon matter overdensity for a given dark matter density perturbation and to different forms of this perturbation.

We start tracing the initial expansion of the perturbation at high redshift when its density contrast is still small. Then we follow decoupling of the perturbation from the Hubble flow and its subsequent collapse and formation of a virialized cloud. We include gas dynamics and various cooling and heating processes operating in the expanding and collapsing cloud. The chemical evolution of the collapsing primordial gas cloud is also accounted for.

After the initial collapse, a virialized gas cloud is formed. The kinetic energy of the infalling gas is dissipated through shocks and the cloud becomes pressure supported. We study the further evolution of the cloud which is determined by its ability to cool sufficiently fast. The most important cooling mechanism for clouds of baryon mass in the range $10^3 - 10^4 M_\odot$ is the radiation of excited $H_2$ molecules. The presence of a small amount of the molecular hydrogen $H_2$ is crucial for triggering the final collapse of low mass clouds which can form the first luminous object in the Universe.

## 2 Nonlinear evolution of a spherically symmetric density perturbation

A major approximation we use is the assumption of spherical symmetry. This assumption is best justified in the case of first objects formed in the Universe which are supposed to originate from the rare highest fluctuations in the primordial density field [8]. It allows us to assess the role of gas dynamics in the collapse of first low-mass clouds.

The spectrum of density fluctuations has more power on small scales, hence the first nonlinear structures are expected to occur on relatively small scales [9]. As we are interested in small scales, much lower than the horizon, we use Newtonian gravity and treat the expansion of the Universe as a hydrodynamical flow. To describe the evolution of a spherically symmetric density perturbation in the nonlinear regime we use Lagrangian coordinates. We divide both baryonic and dark matter into concentric shells. The dynamics of primordial matter is given by the equations below.

The continuity equation for baryonic matter reads

$$\frac{dM_b}{dr_b} = 4\pi r_b^2 \varrho_b, \tag{1}$$

where $r_b$ is the radius of a sphere of mass $M_b$. The radial velocity of the surface of this sphere is

$$\frac{dr_b}{dt} = v_b, \tag{2}$$

and the acceleration satisfies the dynamical equation

$$\frac{dv_b}{dt} = -4\pi r_b^2 \frac{dp}{dM_b} - \frac{GM(r_b)}{r_b^2}, \tag{3}$$

where $M(r_b) = M_b(r_b) + M_{dm}(r_b)$ is the total mass within radius $r_b$.

The energy conservation condition for baryonic matter reads

$$\frac{du}{dt} = \frac{p}{\varrho_b^2}\frac{d\varrho_b}{dt} + \frac{\Lambda}{\varrho_b}, \tag{4}$$

where $u$ is the internal energy per unit mass, $p$ is the pressure and $\varrho_b$ is the baryon density. The last term in the eq.(4) describes cooling/heating of the gas, with $\Lambda$ being the energy absorption (emission) rate per unit volume.

We use the equation of state of the ideal gas

$$p = (\gamma - 1)\varrho_b u, \tag{5}$$

where $\gamma = 5/3$, as the primordial baryonic matter after recombination is assumed to be composed of monoatomic hydrogen and helium with a small (but very important) admixture of molecular hydrogen $H_2$.

Dynamics of dark matter is simpler, as we assume it to be collisionless. The continuity equation is

$$\frac{dM_{dm}}{dr_{dm}} = 4\pi r_{dm}^2 \varrho_{dm}, \tag{6}$$

where $r_{dm}$ is the radius of dark matter sphere of mass $M_{dm}$. The radial velocity of this sphere is

$$\frac{dr_{dm}}{dt} = v_{dm}, \tag{7}$$

and the acceleration reads

$$\frac{dv_{dm}}{dt} = -\frac{GM(r_{dm})}{r_{dm}^2}. \tag{8}$$

To solve the above equations we must specify the cooling/heating function $\Lambda$ and the the initial conditions.

## 3 Initial conditions

Let us begin with the initial conditions. We start to follow the evolution of the perturbation soon after the recombination at a sufficiently high redshift that the perturbation is still in the linear regime. We choose the initial redshift to be $z_i = 500$ as in [5]. It corresponds to the time $t_i = 1.1 \times 10^6$ y after the singularity.

We use two initial density profiles: the perturbation used by Haiman, Thoul and Loeb [5], and the commonly used Gaussian perturbation. The density profiles of baryonic and dark matter perturbations used by Haiman, Thoul and Loeb [5] are of the form

$$\varrho_i(r) = \Omega_i \varrho_c (1 + \delta_i \frac{\sin kr}{kr}), \tag{9}$$

where $i = b, dm$ and $\varrho_c$ is the critical density of the Universe, $\varrho_c = 3H^2/8\pi G$ with $H$ being the actual value of the Hubble parameter. The quantities $\delta_b$ and $\delta_{dm}$ measure, respectively, the baryon and dark matter density enhancement with respect to the mean densities $\bar{\varrho}_b = \Omega_b \varrho_c$ and $\bar{\varrho}_{dm} = \Omega_{dm} \varrho_c$.

For the profile (9) there exist two distinguished values of the radius, $r_0$ and $r_z$ which correspond, respectively, to the first zero and the first minimum of the function $sin(kr)/kr$. Inside the sphere of radius $r_0 = \pi/k$ which contains mass $M_0$, the local density contrast is positive. The mass $M_0$ and the radius $r_0$ will be referred to as the cloud mass and the cloud radius, respectively. The local density contrast is negative for $r_z > r > r_0$, with the average density contrast vanishing for the sphere of radius $r_z = 4.49341/k$ with the mass $M_z$. According to the gravitational instability theory in the expanding Universe, the shell of radius $r_z$ will expand together with the Hubble flow not suffering any additional deceleration. It can thus be regarded as the boundary of the perturbation and the mass $M_z$ will be referred to as the bound mass.

We have made also some calculations with the Gaussian form of the initial overdensity:

$$\varrho_i(r) = \Omega_i \varrho_c \left[ 1 + \delta_i \exp\left( \frac{-r^2}{2R_f^2} \right) \right]. \tag{10}$$

(e.g. [10]), and we define the mass of the cloud $M_0$ as the mass inside the sphere of radius $2R_f$ [11].

As the initial velocity we use the Hubble velocity for baryon matter,

$$v_b(r) = Hr, \tag{11}$$

whereas for dark matter the initial velocity is [5]

$$v_{dm}(r) = Hr(1 - \frac{1}{3} < \delta_{dm} >_r). \tag{12}$$

The expression in brackets indicates averaging over the sphere of radius r. The slower expansion of dark matter at $z_i = 500$ results from the fact that the dark matter perturbations start to grow earlier than do the baryon matter ones.

Finally, the amplitudes of baryon and dark matter perturbations, $\delta_b$ and $\delta_{dm}$ should be specified. To do so one should use the power spectrum corresponding to the initial redshift $z_i = 500$ that provides rms density fluctuations at a given mass $M_0$. For Cold Dark Matter model we use the spectrum due to Bardeen et al. [12]. One should remember that the actual value of the rms density fluctuation $\sigma(z, M_0)$ depends on the shape of the window over which the density is averaged. However, this dependence is quite weak. For example, $\sigma(z_i, 100M_\odot)$ is 0.110 and 0.115 for top-hat and Gaussian windows, respectively [5]. Corresponding values for $M_0 = 10^4 M_\odot$ are $\sigma(z_i, M_0) = 0.104$ and $\sigma(z_i, M_0) = 0.100$, for top-hat and Gaussian windows, respectively [5].

There is considerable uncertainty in the initial value of the baryon density enhancement as the baryon density perturbations start to grow only after the recombination. Below we treat the ratio of baryon to dark overdensity as a phenomenological parameter that is not well known. In our calculations we use a few values of $\delta_b/\delta_{dm}$ in order to assess the sensitivity of the results to a particular value of this parameter.

The Hubble constant value used in the calculations is $H_0 = 50 km/sMpc$.

# 4 Baryonic matter components, chemical reactions and thermal effects

To specify the cooling/heating function $\Lambda$ in Eq.(4) one should include all relevant thermal and chemical processes in the primordial gas. There are many papers discussing the most important contributions to the function $\Lambda$ (see e.g.[6]). We have collected for completeness useful formulae from various sources in Appendix B.

The primordial gas consists of neutral atoms and molecules, ions and free electrons. In this paper we have taken into account nine species: H, $H^-$, $H^+$, He, $He^+$, $He^{++}$, $H_2$, $H_2^+$ and $e^-$. Some authors (e.g. Galli and Palla [Gal98]) include also deuterium and lithium.

It is useful to introduce the mass fraction $y_i$ for each component $i$

$$y_i = \frac{\mu_i n_i}{\varrho_b}, \tag{13}$$

where $n_i$ is the number density and $\mu_i$ is the molecular mass of the species $i$. The abundance of various species can, generally, change with time as the chemical reactions between species occur and the ionization and dissociation photoprocesses take place in the hot gas. The chemical reactions include such processes as e.g. the ionization of hydrogen and helium by electrons, the recombination of ions with electrons, the formation of negative hydrogen ions, the formation of $H_2$ molecules, etc. The full list of relevant chemical reactions is given in the Appendix B. Photoprocesses include ionization of neutral hydrogen $H$ and helium $He$ and $He^+$ by photons, and dissociation of negative hydrogen ions $H^-$ and $H_2$ molecules by photons.

Time evolution of the number density of the component $n_i$ is described by the kinetic equation:

$$\frac{dn_i}{dt} = \sum_{l=1}^{9}\sum_{m=1}^{9} a_{lmi} k_{lm} n_l n_m + \sum_{j=1}^{9} b_{ji}\kappa_j n_j. \tag{14}$$

At the right-hand side of the equation the first component describes chemical reactions and the other one describes photoionization and photodissociation. The coefficients $k_{lm}$ are reaction rates, the quantities $\kappa_n$ are photoionization or photodissociation rates and $a_{lmi}$ and $b_{ji}$ are numbers equal to 0, $\pm 1$ or $\pm 2$ depending on the reaction.

All reaction rates, photoionization and photodissociation rates are given in the Appendix B.

The cooling (heating) function $\Lambda$ includes terms due to such processes as the collisional ionization of $H, He$ and $He^+$, the recombination to $H, He$ and $He^+$, the collisional excitation of $H$ and $He^+$, Bremsstrahlung, the Compton cooling and the cooling due to $H_2$ molecules. The formulae for the heating/cooling contributions of various processes are given in the Appendix B. They were taken from [5], [13] and [14].

The cooling function given in the Appendix B is a general one and can be applied in a wide range of temperatures and densities encountered in cosmological objects. One should note that for low mass objects which have virial temperatures of the order of a few hundred K, only a limited number of reactions are important. Some authors attempt to select only those reactions which are relevant in this restricted temperature range. These are so-called *minimal models* proposed by Tegmark et al. [7] and by Abell et al. [13]. These approximations seem to be, however, too crude for our purpose. In the calculations reported here we decided to include most of the relevant reactions and processes.

## 5 The role of molecular hydrogen $H_2$

One of necessary conditions for a virialized gas cloud to collapse is the presence of an effective cooling mechanism. For high mass clouds that have virial temperatures of the order of $10^5$K or greater, the line emission is the efficient cooling mechanism. Also other processes listed in the Appendix B can contribute. However, the virial temperature of gas clouds that have masses of order of $10^3$ $M_\odot$ is only a few hundred Kelvins. The only known mechanism that may be effective in such temperatures is so-called $H_2$ cooling, i.e. cooling by radiation of excited rotational and vibrational states of $H_2$ molecules.

The primordial gas is thought to include a small admixture of $H_2$ molecules. The initial fraction of $H_2$ is very small, of the order of $10^{-6}$. The $H_2$ molecules may be created via two channels, called $H^-$ channel

$$\begin{aligned} H + e^- &\rightarrow H^- + h\nu \\ H + H^- &\rightarrow H_2 + e^- \end{aligned}$$

and the $H_2^+$ channel

$$\begin{aligned} H + H^+ &\rightarrow H_2^+ + h\nu \\ H_2^+ + H &\rightarrow H_2 + H^+. \end{aligned}$$

Both of these channels can operate because the recombination of cosmic plasma is not complete [17]. There is some residual fraction of unrecombined electrons and positive hydrogen ions left in the primordial gas after recombination, at the level of $10^{-4}$ (at $z \sim 100$ [17]). The $H^-$ channel is not very effective at redshifts $z > 100$ as the $H^-$ molecule is easily photodissociated by photons of CBR. At lower redshifts this channel dominates the production of $H_2$ molecules.

The fraction of molecular hydrogen $H_2$ in gas clouds which collapse becomes higher than the initial value $\sim 10^{-6}$. With increasing density in the collapse regions the fraction of molecular hydrogen increases to about $10^{-4} - 10^{-3}$ [17].

## 6 Numerical code

The dynamical equations (1)-(8) are solved numerically. At each timestep also the chemical composition of the gas is updated by solving Eq.(14) and the appropriate value of the cooling function $\Lambda$ is calculated. We based our numerical code on the code described by Thoul and Weinberg [11], which is the standard, second-order accurate, Lagrangian finite-difference scheme.

We handle timesteps and central boundary conditions in the way proposed by Thoul and Weinberg [11]. For dark matter, to avoid the unphysical collapse to black hole which is an artefact of spherically symmetric calculations, we treat the center as a hard sphere of some "small" radius $r_c$. In order not to affect the results of calculations the value of $r_c$ should be much less than any other characteristic radius in the problem but it should not be too small because smaller $r_c$ means worse energy conservation and longer computation time. We have compared calculations with a few different values of $r_c$ and it seems to be a good idea to choose $r_c$ similar to the initial radius of the most innermost dark matter shell.

In the collapse of baryon matter one encounters the formation of shocks. In our code shocks are treated with the artificial viscosity technique [15].

When writing the code we have faced a problem how to deal with the bounce of dark matter shells off the hard sphere. Let's assume, that for the step $n$ the shell $i$ has radius $r_{dm,i}^n$ and velocity $v_{dm,i}^{n-1/2}$ (in this scheme velocities are taken in half-time between iterations).

In case there is no bounce for the step $n+1$ the velocity and radius should be

$$v_{dm,i}^{n+1/2} = v_{dm,i}^{n-1/2} - \frac{Gm_i^n}{(r_{dm,i}^n)^2} dt^n \tag{15}$$

and

$$r_{dm,i}^{n+1} = r_{dm,i}^n + v_{dm,i}^{n+1/2} dt^{n+1/2}, \tag{16}$$

where $m_i^n$ is the total mass (baryonic and dark) inside $r_i^n$ for $n$-th iteration. Now let us assume that the value $r_{dm,i}^{n+1}$ turns out to be less than $r_c$. Naively, we should leave the same radius and simply change the sign of velocity

$$r_{dm,i}^{n+1} \longrightarrow r_{dm,i}^{n+1} \tag{17}$$

and

$$v_{dm,i}^{n+1/2} \longrightarrow -v_{dm,i}^{n+1/2}. \tag{18}$$

However, we must remember that velocities are taken in half-time between iterations and such simple operation may lead (and leads) to incorrect results. Instead, we should take the "old" value of $r_i$ and reverse velocity:

$$r_{dm,i}^{n+1} \longrightarrow r_{dm,i}^n = r_{dm,i}^{n+1} + (r_{dm,i}^n - r_{dm,i}^{n+1}) \tag{19}$$

and

$$v_{dm,i}^{n+1/2} \longrightarrow -v_{dm,i}^{n+1/2}. \tag{20}$$

This procedure assures proper time iterations. Results obtained using this method will be labelled with "M".

Haiman [21] has suggested another solution:

$$r_{dm,i}^{n+1} \longrightarrow r_{dm,i}^{n+1} \tag{21}$$

and

$$v_{dm,i}^{n+1/2} \longrightarrow -v_{dm,i}^{n+1/2} + \frac{Gm_i^n}{(r_{dm,i}^n)^2} dt^n, \tag{22}$$

which gives the same $r_i$ but adds to $v_i$ some extra outward velocity. This shift is necessary because radii and velocities are taken in slightly different times, e.g. $v_{b,i}^{n+1/2}$ is taken $dt/2$ later than $r_{b,i}^n$. Further curves showing solutions obtained with this method will be labelled with "H". Both methods are equivalent and give the same results.

The choice of the timestep is of great practical importance. For a given shell one can define the following time scales [11]:

$$\tau_{dyn,i}^b = \sqrt{\frac{\pi^2 r_{b,i}^3}{8GM_i}}, \tag{23}$$

$$\tau_{cool,i} = \left| \frac{u_i \varrho_i}{\Lambda_i} \right|. \tag{24}$$

$$\tau_{Cour,i} = \left| \frac{r_{b,i} - r_{b,i-1}}{\sqrt{\gamma(\gamma-1)u_i}} \right|, \tag{25}$$

and

$$\tau^b_{vel,i} = \left| \frac{r_{b,i} - r_{b,i-1}}{v_{b,i} - v_{b,i-1}} \right|, \tag{26}$$

For baryonic matter we use as the timestep the minimum value

$$dt_b = \min_i \{c_d \tau^b_{dyn,i}, c_C \tau_{Cour,i}, c_c \tau_{cool,i}, c_v \tau^b_{vel,i}\}, \tag{27}$$

where $c_d$, $c_C$, $c_c$ and $c_v$ are some safety constants. We have used the following values: $c_d = 0.02$, $c_C = 0.2$, $c_c = 0.1$, $c_v = 0.05$ [11].

For the dark component we use the timestep

$$dt_{dm} = \min_i \{c_d \tau^{dm}_{dyn,i}, 4 c_v \tau^{dm}_{vel,i}\}, \tag{28}$$

where

$$\tau^{dm}_{dyn,i} = \sqrt{\frac{\pi^2 r^3_{dm,i}}{8GM_i}}, \tag{29}$$

and

$$\tau^{dm}_{vel,i} = \left| \frac{r_{dm,i} - 0.9 r_c}{v_{dm,i}} \right|, \tag{30}$$

where $c_d$ and $c_v$ are defined above and $r_c$ is the radius of the hard sphere. Because the calculations for the baryonic matter are relatively long, if $dt_{dm} < dt_b$ we were doing a few iterations for the dark matter during one iteration for the baryonic matter.

Because the baryons were locked to the CBR until the epoch of recombination, it is necessary to choose lower values of the initial overdensities for baryons than for dark matter. The proper value of the baryon matter overdensity is not well determined. Haiman, Thoul and Loeb [5] have chosen somewhat arbitrary value $\delta_{b,i} = 0.1\delta_{dm,i}$. To test the sensitivity of the calculations to this assumption we have made some calculations for different values of $\delta_{b,i}$. We used higher value $\delta_{b,i} = 0.2\delta_{dm,i}$ corresponding to somewhat faster growth of baryonic fluctuations after recombination. We also used $\delta_{b,i} = 0$ in order to see if dark matter perturbations can trigger collapse of gas clouds which are initially uniform.

To check our numerical code we have chosen the initial parameters close to parameters used by Haiman, Thoul and Loeb [5] who have made a detailed study of density peaks in the $\Omega_b = 0.1$ and $\Omega_{dm} = 0.9$ Universe with the Hubble parameter $H_0 = 50\mathrm{km/(s \cdot Mpc)}$. We have found that the best way to check the numerical code was to reproduce results of Haiman et al. for the cloud mass $M_0 = 1000 M_\odot$ and $\delta_{dm,i} = 0.39$. In this case only the most innermost shells collapse at $z \simeq 10$ and a tiny change in conditions could prevent them from collapsing or make also outer shells to collapse. In other cases considered in [5] either there was no collapse after virialization ($M_0 = 500 M_\odot, \delta_{dm,i} = 0.26$ and $M_0 = 1000 M_\odot, \delta_{dm,i} = 0.26$) or the collapse was quite fast ($M_0 = 5000 M_\odot, \delta_{dm,i} = 0.26$).

The cosmological observable is the redshift. To convert time in our evolutionary calculations into redshift we give the appropriate formula in Appendix A.

# 7 Results and conclusions

We expect that as the dark matter dominates in the model the behaviour of dark matter shells will play the crucial role in the cloud collapse. Due to our assumptions, dark matter is collisionless, so there is no energy loss mechanism apart from possible gravitational energy exchange.

The expected evolution of the dark matter shells in the absence of baryonic matter is that their radii increase to some maximal value, then the shells collapse and after some oscillations due to bounces off the hard sphere the dark matter cloud becomes stationary. In the presence of baryonic matter the behaviour of dark matter shells should be similar because the amount of baryonic matter is much less than the amount of dark matter.

The expected behaviour of baryon matter shells is that after reaching maximum radii, the shells collapse and the shock develops at some stage due to pressure crowding of neighbouring shells [5]. The shock stops the collapse and the baryon shells virialize. After virialization they can undergo the final collapse.

Results of our calculations are displayed in Figs. $1-11$. In Fig.1a and Fig.1b we show the evolution of dark matter shells and baryon matter shells for the cloud mass $M_0 = 1000 M_\odot$ and $M_0 = 5000 M_\odot$, respectively. The values of the dark matter density enhancement are, respectively, $\delta_{dm,i} = 0.39$ and $\delta_{dm,i} = 0.26$.

The curves displayed in Fig. 1a and Fig. 1b correspond to radii of 10 shells of baryon matter and dark matter. The innermost shell encloses 7% of the bound mass, next shells enclose, respectively, $17\%, 27\%, ..., 97\%$ of the bound mass. This fractional division of mass applies to both dark matter and baryon matter shells. In the following figures we display always shells containing the same fraction of mass as in Figs. 1a and 1b. The initial density perturbation has the form (9) used by Haiman, Thoul and Loeb [5]. In the following this form will be referred to as the sinusoidal perturbation. Most of the results displayed below correspond to this form of the initial perturbation.

Dark matter shells expand to some maximum radius and then collapse to about a half of this value. The radius of the hard sphere is $r_c = 0.1 r_0$. The behaviour of dark matter is very similar for both values of the cloud mass. This means that the evolution of dark matter is not very sensitive to the mass of the cloud. In contrast, the behaviour of baryon matter shells strongly depends on the cloud mass. In the case of Fig.1a, corresponding to the run 7 in [5], baryonic shells expand to maximum radii then virialize, but only the innermost shell undergoes the final collapse at redshift $z = 9$. For higher cloud mass, Fig.1b, many inner shells undergo the final collapse after virialization, starting at redshift $z \sim 20$. We see that higher mass clouds start to collapse at higher redshift than those of lower mass.

Figs. 2a and 2b show the comparison of the two methods H and M of the correct implementation of the bounce of the dark matter shells off the hard sphere in the numerical calculations. The results for both methods are indistinguishable within numerical errors. This proves that both methods are equivalent.

Results presented in Figs. 2a and 2b correspond to the case of neglecting the radiation contribution to the mass density at the initial redshift, $z_i = 500$. When this contribution is included, the expansion rate of the Universe at the redshift $z_i$ slightly changes. This affects somewhat the behaviour of dark and baryon matter density perturbations. The effect is shown in Figs. 3a and 3b where the evolution of dark and baryon matter shells is presented. As one can see with the radiation contribution included the shells stop to expand at somewhat lower redshift than in case of no radiation contribution. This is a result of higher expansion rate at the initial redshift. Figs. 4a and 4b show the same, but for the Gaussian perturbation.

The influence of the $H_2$ cooling on the collapse of baryon matter is shown in Figs. 5-7. The role of this cooling mechanism is crucial for triggering the final collapse of baryon matter after virialization. In Figs. 5a and 5b we show the evolution of baryon and dark matter shells, respectively, for $M_0 = 1000 M_\odot$ and $\delta_{dm,i} = 0.39$. The dashed curves correspond to the case of no $H_2$ cooling and the solid curves are for the case of operating $H_2$ cooling.

The innermost baryon shell in case of no molecular hydrogen cooling does not shrink any more after virialization. It becomes gravitationally stable supported by the pressure of the warm gas, which, in absence of $H_2$ cooling cools very slowly. When the $H_2$ cooling is included, the

shell after virialization begins to shrink and around $z \sim 10$ undergoes the final collapse. The $H_2$ cooling does not affect dark matter shells as is seen in Fig. 5b. The shells evolve in the same way irrespective to the presence of $H_2$ cooling mechanism.

The role of $H_2$ cooling is very pronounced in Fig. 6 where the virialized mass and the collapsed mass are shown as functions of redshift, for the same cloud parameters as in Fig. 5a. By virialized mass we mean the mass of the shell that all baryonic shells inside have density greater than $18\pi^2\rho_c$, where $\rho_c$ is the actual mean density of the Universe. The collapsed mass corresponds to shells of mean density exceeding the virialization density by a factor of 100. The virialized object starts to emerge at redshift $z \sim 30$ and by $z \sim 10$ essentially all the cloud mass meets the virialization criteria irrespective to the presence of the $H_2$ cooling. With $H_2$ cooling included about 20 % of the cloud mass collapses by $z \sim 10$ (lower curve in Fig. 6). With no $H_2$ cooling, no shell meets the collapse condition.

In Fig. 7 we show the temperature of shells as a function of redshift. The curves indicating temperatures of baryonic shells behave in an opposite way than the radii of baryonic shells. The temperature falls during expansion and increases in the collapse phase. After virialization the temperature remains rather constant. Oscillations in Fig. 7 are of purely numerical origin. There is only a tiny difference between the cases with and without $H_2$ cooling.

The influence of the initial baryon overdensity on the collapse behaviour of baryonic shells is shown in Figs. 8a and 8b. The evolution of shells is essentially identical for $\delta_b$ equal to 0, $0.1\delta_{dm}$ and $0.2\delta_{dm}$. These results indicate that the initial value of the baryon overdensity is not an important parameter of the model. The dark matter perturbations create gravitational potential wells deep enough to trigger collapse of baryon matter even in the case when its density is uniform at the initial redshift.

In Fig. 9 we compare calculations with sinusoidal and Gaussian perturbations. For the sinusoidal perturbation the inner shells collapse faster and outer ones collapse slower than for the Gaussian perturbation. This behaviour can be easily understood. For the Gaussian shape of the perturbation at the center the density falls faster but the overdensity is always positive while for the sinusoidal perturbation for $r > r_0$ overdensity starts to be negative and for $r = r_z$ the mean overdensity is equal to zero. For the Gaussian perturbation mean overdensity is always positive.

Fig. 10 shows the time evolution of density profiles of both baryonic and dark components of collapsing clouds. We show curves corresponding to the initial redshift $z_i = 500$, then to some lower redshifts and the last curves are for $z = 8$. Radii and densities are in comoving coordinates. For both components we can see the evolution from an almost flat initial density distribution with a tiny overdensity to an almost power-law profile $\varrho \sim r^{-2.25}$ near the center predicted by Bertschinger [16] for a self-similar relaxation. Dark matter distribution follows this behaviour very closely.

The abundance of various species as a function of redshift is shown in Fig. 11. The results correspond to the shell of mass $M = 0.12M_z$ of the same cloud as in Figs. 5-10. One can notice the increase of the amount of $H_2$ molecules at later redshift when the shell collapses. This makes $H_2$ cooling more efficient, triggering the final collapse of inner shells.

To conclude, we have studied the nonlinear collapse of low-mass density perturbations in the CDM cosmology. The first gas clouds that collapse in this model have baryon mass of the order of $10^3 - 10^4 M_\odot$. These objects which are the first bound and luminous objects in the Universe correspond to $3\sigma$ perturbations of the lowest mass which can still effectively cool. The virial temperatures of these clouds are low and the crucial role is played by the $H_2$ cooling mechanism which triggers the final collapse after virialization.

In this paper we have extended the analysis of [5] to investigate the role of the initial baryon overdensity $\delta_{b,i}$ for a given dark matter perturbation. We have found that the collapse of baryon matter shells is essentially independent of the value of $\delta_{b,i}$. The shells collapse in the same way

for $\delta_{b,i} = 0.2\delta_{dm,i}$ and for $\delta_{b,i} = 0$. This indicates that the dark matter perturbations create potential wells deep enough to induce the collapse of baryon clouds which are of uniform density at the initial redshift, soon after recombination. We have also calculated the evolution of clouds which have initially a Gaussian form. There are some differences in the collapse of subsequent shells of baryon and dark matter as compared to the case of sinusoidal perturbations (Fig. 9) resulting from somewhat different density distributions in both cases. We have also included the radiation contribution to the mass density of the Universe. This changes somewhat results obtained with no radiation contribution included.

We are grateful to Dr. Zoltan Haiman for very useful discussions.

## Appendix A Relations between H, t and z

The mass density $\varrho$ of the Universe has at least two components: $\varrho_M$, the matter contribution, which is proportional to $(1+z)^3$, and $\varrho_r$the radiation contribution, which behaves as $(1+z)^4$. Usually in the matter-dominated era the radiation component is neglected and vice versa but, however, the presence of the radiation may affect the results. In some models, also cosmological constant contributes to $\varrho$. The corresponding energy density $\varrho_\Lambda$ does not change with redshift.

The exact formula for $H(z)$ in cosmological models with matter, radiation and cosmological constant reads

$$H = H_0\sqrt{\Omega_M(z+1)^3 + \Omega_r(z+1)^4 + \Omega_\Lambda + (z+1)^2(1-\Omega_M-\Omega_r-\Omega_\Lambda)}. \qquad (31)$$

where $\Omega_i = \varrho_i/\varrho_c$ with $\varrho_c$ being the actual critical density of the Universe. Thus, the relation between time and redshift is

$$H_0 t(z) = \int_z^\infty \frac{(z+1)^{-1}dz}{\sqrt{\Omega_M(z+1)^3 + \Omega_r(z+1)^4 + \Omega_\Lambda + (z+1)^2(1-\Omega_M-\Omega_r-\Omega_\Lambda)}} \qquad (32)$$

This formula, but without $\Omega_r$, may be found e.g. in Peebles [17], eq. 13.9.

Equation (32) allows us to calculate the time since the Big Bang $t$ from redshift $z$ for cosmological models with given $\Omega_M$ and $\Omega_\Lambda$. Unfortunately, analytical solutions may be found in some special cases only – e.g. if $\Omega_r = 0$ and $\Omega_M + \Omega_\Lambda = 1$ (flat Universe without radiation). To perform numerical integration we have used three functions from *Numerical recipes in C* [18] (`midpnt` and `midinf`, called by function `qromo`). We have compared results of numerical and analytical calculations for models with $\Omega_M + \Omega_\Lambda = 1$ and $\Omega_\Lambda = 0$, for values of $\Omega_M$ from 0.01 to 1. In the first case, numerical values were systematically greater by the factor of 1.0000648. In the second case, this factor was a bit greater : 1.0000648 for $\Omega_M = 1.00$, 1.0000701 for $\Omega_M = 0.24$, 1.0001048 for $\Omega_M = 0.03$ and 1.0001564 for $\Omega_M = 0.01$. Anyway, for $\Omega_M \geq 0.25$ it was less than 1.00007 and we have decided that this accuracy is enough for our purposes. Let us stress that the effects of non-zero $\Omega_r$ are much greater, especially for low values of $\Omega_M$.

## Appendix B Cooling functions, reaction rates and cross-sections

We have adopted contributions to the cooling function $\Lambda$, reaction rates and cross-sections from Cen [19], Haiman, Thoul and Loeb [5], Tegmark et al. [7], Galli and Palla [14] and Abel et al. [13]. The cooling function $\Lambda$ is in ergs/(s·cm$^3$), reaction rates are in cm$^3$/s and cross-sections in cm$^2$. $T$ is temperature in Kelvins, thermal energy $E = kT$ is in eV, $T_n$ is temperature in $10^n$ K and `Poly` is polynomial function $\mathrm{Poly}(x, a_0, a_1, ...a_n) = a_0x^0 + a_1x^1 + a_2x^2 + ... + a_nx^n$.

**Cooling and heating contributions**
All coefficients in ergs/(s·cm$^3$), from Ref.[5].

a) Collisional ionization of H, He and He$^+$:

$$\Lambda_{\rm H}(T) = 1.27\times10^{-21}T^{\frac{1}{2}}(1+T_5^{\frac{1}{2}})^{-1}\exp(-157809.1/T)n_{\rm e}n_{\rm H} \quad (33)$$

$$\Lambda_{\rm He}(T) = 9.38\times10^{-22}T^{\frac{1}{2}}(1+T_5^{\frac{1}{2}})^{-1}\exp(-285335.4/T)n_{\rm e}n_{\rm He} \quad (34)$$

$$\Lambda_{\rm He^+}(T) = 4.95\times10^{-22}T^{\frac{1}{2}}(1+T_5^{\frac{1}{2}})^{-1}\exp(-631515/T)n_{\rm e}n_{\rm He^+} \quad (35)$$

b) Recombination to H, He and He$^+$:

$$\Lambda_{\rm H^+}(T) = 8.70\times10^{-27}T^{\frac{1}{2}}T_3^{-0.2}(1+T_6^{0.7})^{-1}n_{\rm e}n_{\rm H^+} \quad (36)$$

$$\Lambda_{\rm He^+}(T) = 1.55\times10^{-26}T^{0.3647}n_{\rm e}n_{\rm He^+} \quad (37)$$

$$\Lambda_{\rm He^{++}}(T) = 3.48\times10^{-26}T^{\frac{1}{2}}T_3^{-0.2}(1+T_6^{0.7})^{-1}n_{\rm e}n_{\rm He^{++}} \quad (38)$$

c) Dielectric recombination to He:

$$\Lambda_{\rm He^+}(T) = 1.24\times10^{-13}T^{-1.5}\exp(-470000/T)(1+0.3\exp(-94000/T))n_{\rm e}n_{\rm He^+} \quad (39)$$

d) Collisional excitation of H and He$^+$:

$$\Lambda_{\rm H}(T) = 7.50\times10^{-19}(1+T_5^{\frac{1}{2}})^{-1}\exp(-118348/T)n_{\rm e}n_{\rm H} \quad (40)$$

$$\Lambda_{\rm He^+}(T) = 5.54\times10^{-17}T^{-0.397}(1+T_5^{\frac{1}{2}})^{-1}\exp(-473638/T)n_{\rm e}n_{\rm He^+} \quad (41)$$

e) Bremsstrahlung:

$$g_{\rm ff} = 1.10+0.34\exp(-(5.50-\log T)^2/3.0) \quad (42)$$

$$\Lambda_{\rm Brem}(T) = 1.42\times10^{-27}g_{\rm ff}T^{\frac{1}{2}}n_{\rm e}(n_{\rm H}^+ + n_{\rm He^+} + 4n_{\rm He^{++}}) \quad (43)$$

f) Compton cooling:

$$\Lambda_{\rm Comp}(T) = 1.017\times10^{-37}T_\gamma^4(T-T_\gamma)n_{\rm e} \quad (44)$$

g) $H_2$ cooling [7]:
The total hydrogen density is:

$$n = n_{\rm H} + n_{\rm H^+} + n_{\rm H^-} + 2(n_{\rm H_2} + n_{\rm H_2^+}). \quad (45)$$

The cooling rate in LTE:

$$L^{(lte)} \approx \frac{1}{n}\left[\left(\frac{9.5\times10^{-22}T_3^{3.76}}{1+0.12T_3^{2.1}}\right)\exp(-(0.13/T_3)^3) + 3\times10^{-24}\exp(-0.51/T_3)\right]. \quad (46)$$

The critical hydrogen density is:

$$n_{cr} \equiv \frac{L^{(lte)}}{L^{(n\to0)}}n, \quad (47)$$

where $L^{(n\to0)}$ is the low-density limit of the cooling function, given by [14]:

$$\log L^{(n\to0)} \approx {\rm Poly}(\log T, -103.0, 97.59, -48.05, 10.80, -0.9032). \quad (48)$$

Now we can calculate the cooling function:

$$\Lambda(T) = \frac{L^{(lte)}}{1 + n_{cr}/n}. \tag{49}$$

Radiative $H_2$ cooling is thermodynamically impossible when $T < T_\gamma$ ($T_\gamma$ is the CBR temperature), so it is necessary to use the net cooling rate [7]

$$\Lambda_{H_2}(T) = \Lambda(T) - \Lambda(T_\gamma). \tag{50}$$

It is worth to note that Haiman, Thoul and Loeb [5] have used somewhat different expression

$$\Lambda_{H_2}(T) = \Lambda(T)\frac{T - T_\gamma}{T + T_\gamma}. \tag{51}$$

**Reaction rates**

All coefficients in $\mathrm{cm}^3/\mathrm{s}$.

(1) $H + e^- \rightarrow H^+ + 2e^-$ [5]

$$k_1 = 5.85 \times 10^{-11} T^{\frac{1}{2}} (1 + T_5^{\frac{1}{2}})^{-1} \exp(-157809.1/T)$$

(2) $He + e^- \rightarrow He^+ + 2e^-$ [5]

$$k_2 = 2.38 \times 10^{-11} T^{\frac{1}{2}} (1 + T_5^{\frac{1}{2}})^{-1} \exp(-285335.4/T)$$

(3) $He^+ + e^- \rightarrow He^{++} + 2e^-$ [5]

$$k_3 = 5.68 \times 10^{-12} T^{\frac{1}{2}} (1 + T_5^{\frac{1}{2}})^{-1} \exp(-631515.0/T)$$

(4) $H^+ + e^- \rightarrow H + h\nu$ [5]

$$k_4 = 8.40 \times 10^{-11} T^{-\frac{1}{2}} T_3^{-0.2} (1 + T_6^{0.7})^{-1}$$

(5) $He^+ + e^- \rightarrow He + h\nu$ [19]

$$k_5 = 1.50 \times 10^{-10} T^{-0.6335}$$

(6) $He^{++} + e^- \rightarrow He^+ + h\nu$ [5]

$$k_6 = 3.36 \times 10^{-10} T^{-\frac{1}{2}} T_3^{-0.2} (1 + T_6^{0.7})$$

(7) $H + H^+ \rightarrow H_2^+ + h\nu$ [13]

$$k_7 = \begin{cases} \exp[\mathrm{Poly}(\ln(E), -20.06913897, 0.22898, 3.5998377 \times 10^{-2}, & \\ 4.55512 \times 10^{-3}, -3.10511544 \times 10^{-4}, 1.0732940 \times 10^{-4}, & \\ 8.36671960 \times 10^{-6}, 2.2380623 \times 10^{-7})] & \mathrm{E} > 0.1 \text{ eV} \\ 1.428 \times 10^{-9} & \mathrm{E} \leq 0.1 \text{ eV} \end{cases}$$

(8) $H_2^+ + H \rightarrow H_2 + H^+$ [5]

$$k_8 = 6.40 \times 10^{-10}$$

(9) $H + e^- \rightarrow H^- + h\nu$ [5]

$$k_9 = 5.57 \times 10^{-17} T^{\frac{1}{2}}$$

(10) $H + H^- \rightarrow H_2 + e^-$ [5]

$$k_{10} = 1.30 \times 10^{-9}$$

(11) $H_2^+ + e^- \rightarrow 2H$ [5]

$$k_{11} = 1.68 \times 10^{-8}(T/300)^{-0.29}$$

(12) $H_2^+ + H^- \rightarrow H_2 + H$ [5]

$$k_{12} = 5.00 \times 10^{-6} T^{-\frac{1}{2}}$$

(13) $H^- + H^+ \rightarrow 2H$ [5]

$$k_{13} = 7.00 \times 10^{-7} T^{-\frac{1}{2}}$$

(14) $H_2 + e^- \rightarrow H + H^-$ [5]

$$k_{14} = 2.70 \times 10^{-8} T^{-\frac{3}{2}} \exp(-43000/T)$$

(15) $H_2 + H \rightarrow 3H$ [13]

$$k_{15} = 1.067 \times 10^{-10} T^{2.012} \exp[-(4.463/E)(1 + 0.2472E)^{3.52}]$$

(16) $H_2 + H^+ \rightarrow H_2^+ + H$ [5]

$$k_{16} = 2.4 \times 10^{-9} \exp(-21200/T)$$

(17) $H_2 + e^- \rightarrow 2H + e^-$ [5]

$$k_{17} = 4.38 \times 10^{-10} \exp(-102000/T) T^{0.35}$$

(18) $H^- + e^- \rightarrow H + 2e^-$ [5]

$$k_{18} = 4.00 \times 10^{-12} T \exp(-8750/T)$$

(19) $H^- + H \rightarrow 2H + e^-$ [5]

$$k_{19} = 5.30 \times 10^{-20} \exp(-8750/T) T^{2.17}$$

(20) $H^- + H^+ \rightarrow H_2^+ + e^-$ [13]

$$k_{20} = \begin{cases} 2.291 \times 10^{-10} E^{-0.4} & \text{E} \leq 1.719 \text{ eV} \\ 8.4258 \times 10^{-10} E^{-10.4} \exp(-1.301/E) & \text{E} > 1.719 \text{ eV} \end{cases}$$

**Photoionization and photodissociation cross-sections**

For each reaction there is a threshold frequency $\nu_0$. Cross-sections are in $\text{cm}^2$.

(21) $H + h\nu \rightarrow H^+ + e^-$ [20]

(22) $He^+ + h\nu \rightarrow He^{++} + e^-$

$A_0 = 6.30 \times 10^{-18} \text{cm}^2$, $\varepsilon = \sqrt{\nu/\nu_0 - 1}$, $h\nu_0 = 13.6 Z^2 \text{eV}$, $Z = 1$ for H and $Z = 2$ for He.

$$\sigma_{21,22} = \frac{A_0}{Z^2} \left(\frac{\nu}{\nu_0}\right)^4 \frac{\exp[4 - 4(\arctan\varepsilon)/\varepsilon]}{1 - \exp(-2\pi/\varepsilon)}$$

(23) $He + h\nu \rightarrow He^+ + e^-$ [20]

$$\sigma_{23} = 7.83 \times 10^{-18} \left[1.66 \left(\frac{\nu}{\nu_0}\right)^{-2.05} - 0.66 \left(\frac{\nu}{\nu_0}\right)^{-3.05}\right] \text{cm}^2, \quad \nu_0/c = 1.983 \times 10^5 \text{cm}^{-1}$$

(24) $H^- + h\nu \rightarrow H + e^-$ [13]

$$\sigma_{24} \;=\; 7.928\times10^{5}(\nu-\nu_0)^{3/2}\nu^{-3}\mathrm{cm}^2,\quad h\nu_0 = 0.755\mathrm{eV}$$

(25) $H_2^+ + h\nu \rightarrow H + H^+$ [13]

$$\sigma_{25} \;=\; \begin{cases} 0 & \text{for } h\nu < 15.42\mathrm{eV} \\ 6.2\times10^{-18}h\nu - 9.4\times10^{-17}\mathrm{cm}^2 & \text{for } 15.42\mathrm{eV} \le h\nu < 16.50\mathrm{eV} \\ 1.4\times10^{-18}h\nu - 1.48\times10^{-17}\mathrm{cm}^2 & \text{for } 16.50\mathrm{eV} \le h\nu < 17.7\mathrm{eV} \\ 2.5\times10^{-14}(h\nu)^{-2.71}\mathrm{cm}^2 & \text{for } h\nu \ge 17.7\mathrm{eV} \end{cases}$$

(26) $H_2 + h\nu \rightarrow H_2^+ + e^-$ [13]

$$\log\sigma_{26} \;=\; \mathrm{Poly}(h\nu,\quad -1.6547717\times10^{6}, 1.8660333\times10^{5}, -7.8986431\times10^{3}, 148.73693, -1.0513032),\quad h\nu_0 = 2.65\mathrm{eV}$$

(27) $H_2 + h\nu \rightarrow H_2^* \rightarrow 2H$ [5], [13]

$$\sigma_{27} \;=\; 3\times10^{-22}\mathrm{cm}^2 \;\text{ for } 12.24\mathrm{eV} \le h\nu < 13.51\mathrm{eV}$$

(28) $H_2 + h\nu \rightarrow 2H$ [13]

$$\sigma_{28} \;=\; \frac{1}{y+1}(\sigma_{28}^{L0}+\sigma_{28}^{W0}) + \frac{y}{y+1}(\sigma_{28}^{L1}+\sigma_{28}^{W1}),$$

where

$$\begin{aligned}
\sigma_{28}^{L0} &= 10^{-18}\mathrm{cm}^2 \times \begin{cases} \mathrm{dex}(15.1289 - 1.05139h\nu) & 14.675\mathrm{eV} < h\nu < 16.820\mathrm{eV} \\ \mathrm{dex}(-31.41 + 1.8042\times10^{-2}(h\nu)^3 - 4.2339\times10^{-5}(h\nu)^5) & 16.820\mathrm{eV} \le h\nu < 17.6\mathrm{eV} \end{cases} \\
\sigma_{28}^{W0} &= 10^{-18}\mathrm{cm}^2 \times \mathrm{dex}(13.5311 - 0.9182618h\nu) \quad 14.675\mathrm{eV} < h\nu < 17.7\mathrm{eV} \\
\sigma_{28}^{L1} &= 10^{-18}\mathrm{cm}^2 \times \begin{cases} \mathrm{dex}(12.0218406 - 0.819429h\nu) & 14.159\mathrm{eV} < h\nu < 15.302\mathrm{eV} \\ \mathrm{dex}(16.04644 - 1.82438h\nu) & 15.302\mathrm{eV} < h\nu < 17.2\mathrm{eV} \end{cases} \\
\sigma_{28}^{W1} &= 10^{-18}\mathrm{cm}^2 \times \mathrm{dex}(12.87367 - 0.85088597h\nu) \quad 14.159\mathrm{eV} < h\nu < 17.2\mathrm{eV}
\end{aligned}$$

where $y$ is the ortho-$H_2$ to para-$H_2$ ratio, $y = 3$ [7], [14].

**References:**


[1] Hsiao-Wen Chen, KM. Lanzetta, S. Pascarelle, Nature, **398**, 586 (1999)

[2] D.L. Clements, S.A. Eales, A.C. Backer, MNRAS, **308**, L11 (1999)

[3] A. Loeb, *The First Stars and Quasars in the Universe*, Science With The NGST (Next Generation of Space Telescope), ASP Conference Series **133**, 73 (1998)

[4] A. Ferrara, S. Marri, *The First Structures in the Universe: Pop III Objects*, The Young Universe: Galaxy Formation and Evolution at Intermediate and High Redshift. Edited by S. D'Odorico, A. Fontana, and E. Giallongo. ASP Conference Series, **146**, 263 (1998)

[5] Z. Haiman, A.A. Thoul, A. Loeb, ApJ, **464**, 523 (1996)

[6] N. Katz, D.H. Weinberg, L. Hernquist, ApJ Suppl. Series, **105**, 19 (1996)

[7] M. Tegmark, J. Silk, M.J. Rees, A. Blanchard, T. Abel, F. Palla, ApJ, **474**, 1 (1997)

[8] D.J. Eisenstein, A. Loeb, ApJ, **443**, 11 (1995)

[9] A.D. Miller et al, AAS **195**, 5508 (1999)

[10] A.R. Liddle, D.H. Lyth, Phys. Rept., **231**, 1 (1993)

[11] A.A. Thoul, D.H. Weinberg, ApJ, **442**, 480 (1995)

[12] J.M. Bardeen, J.R. Bond, N. Kaiser, A.S. Szalay, ApJ, **304**, 15 (1986)

[13] T. Abel, P. Anninos, Yu Zhang, M.L. Norman, New Astron., **2**, 181 (1997)

[14] D. Galli, F. Palla, Astron. Astrophys., **335**, 403 (1998)

[15] R. Richtmyer, K.W. Morton, *Difference methods for Initial-Value Problems*, Interscience Publishers, New York (1967)

[16] E. Bertschinger, ApJ Suppl. S., **58**, 39 (1985)

[17] P.J.E. Peebles, *Principles of Physical Cosmology*, Princeton University Press, Princeton, New Jersey (1993)

[18] W.H. Press, S.A. Teukolsky, W.T. Vetterling, B.P. Flannery *Numerical Recipes in C. The Art of Scientific Computing. Second Edition*, Cambridge University Press (1996)

[19] R. Cen, ApJ Suppl. S., **78**, 341 (1992)

[20] D.E. Osterbrock, *Astrophysics of Gaseous Nebulae*, Freeman & Co: San Francisco, CA (1974)

[21] Z. Haiman, private communication

## Figures

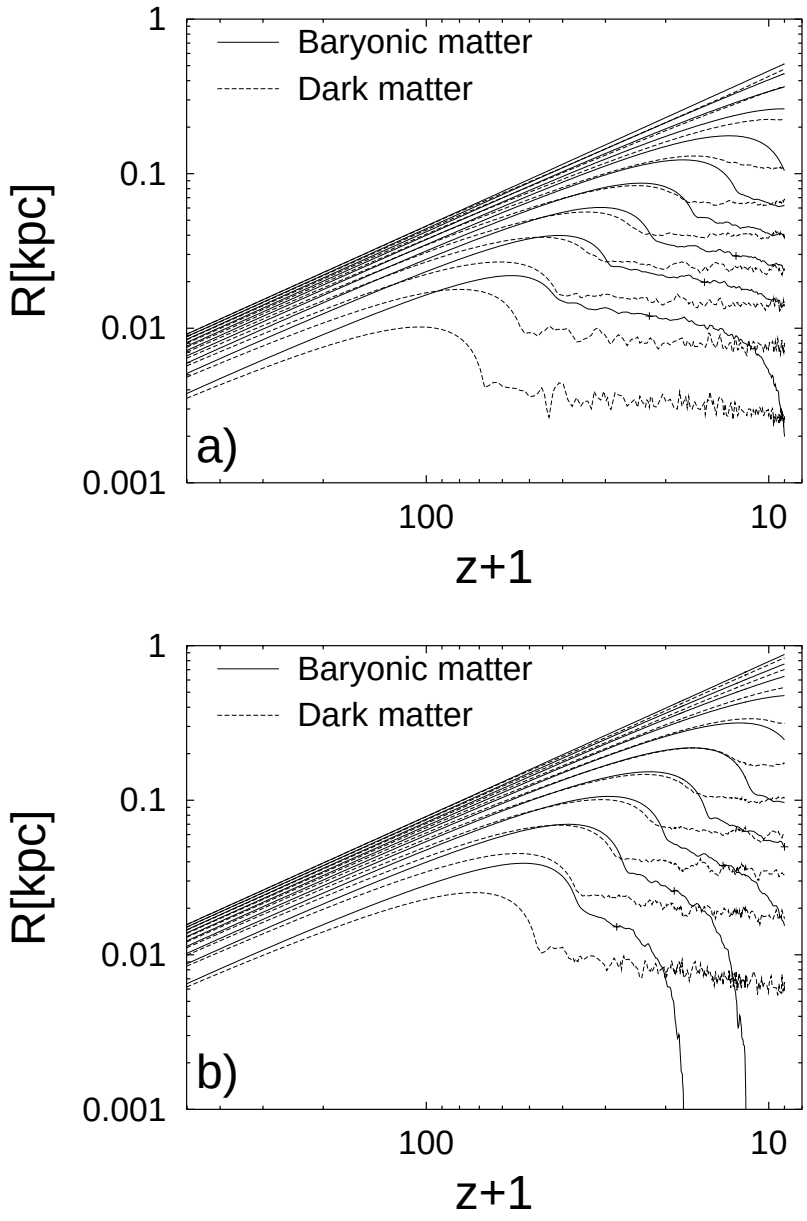


Fig. 1. Shell radii as functions of redshift for baryon matter and dark matter. The plots a and b correspond, respectively, to 1000 $M_\odot$ and 5000 $M_\odot$ clouds.

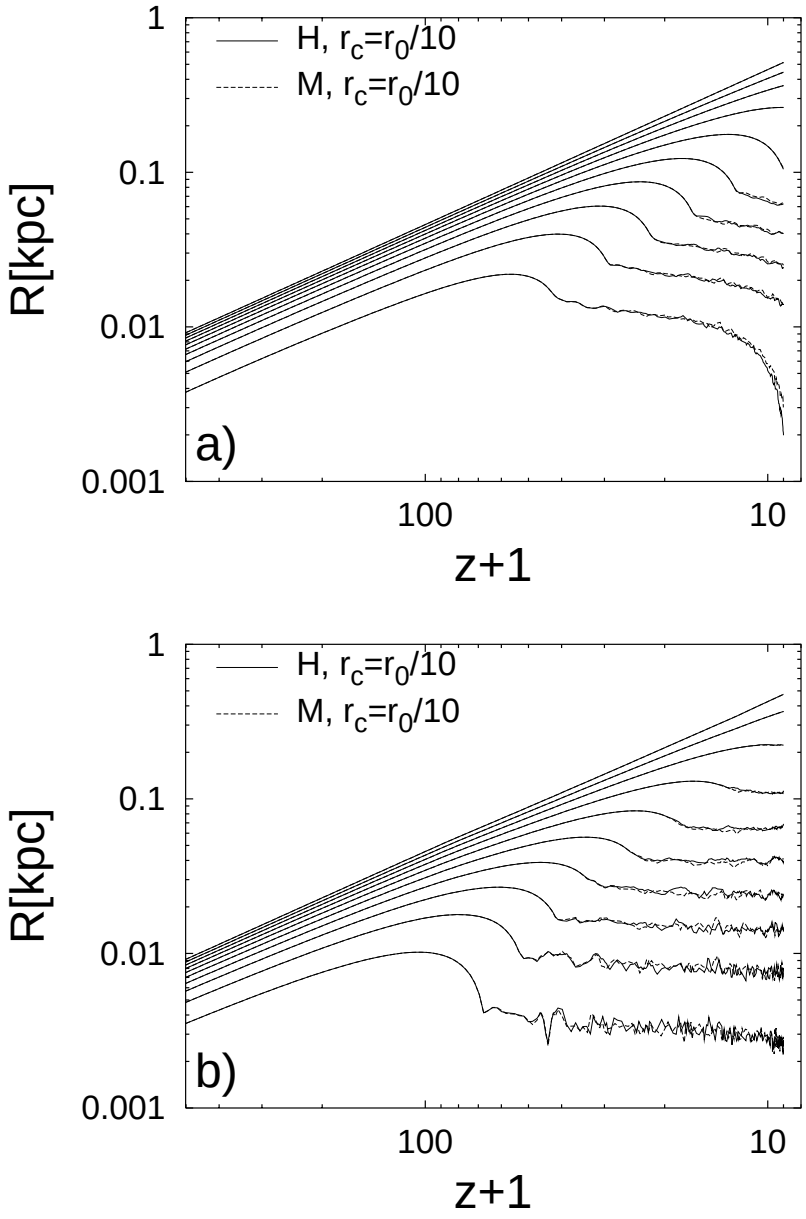


Fig. 2. The evolution of shell radii calculated with the H and M methods. Plots a and b correspond to baryon matter and dark matter, respectively.

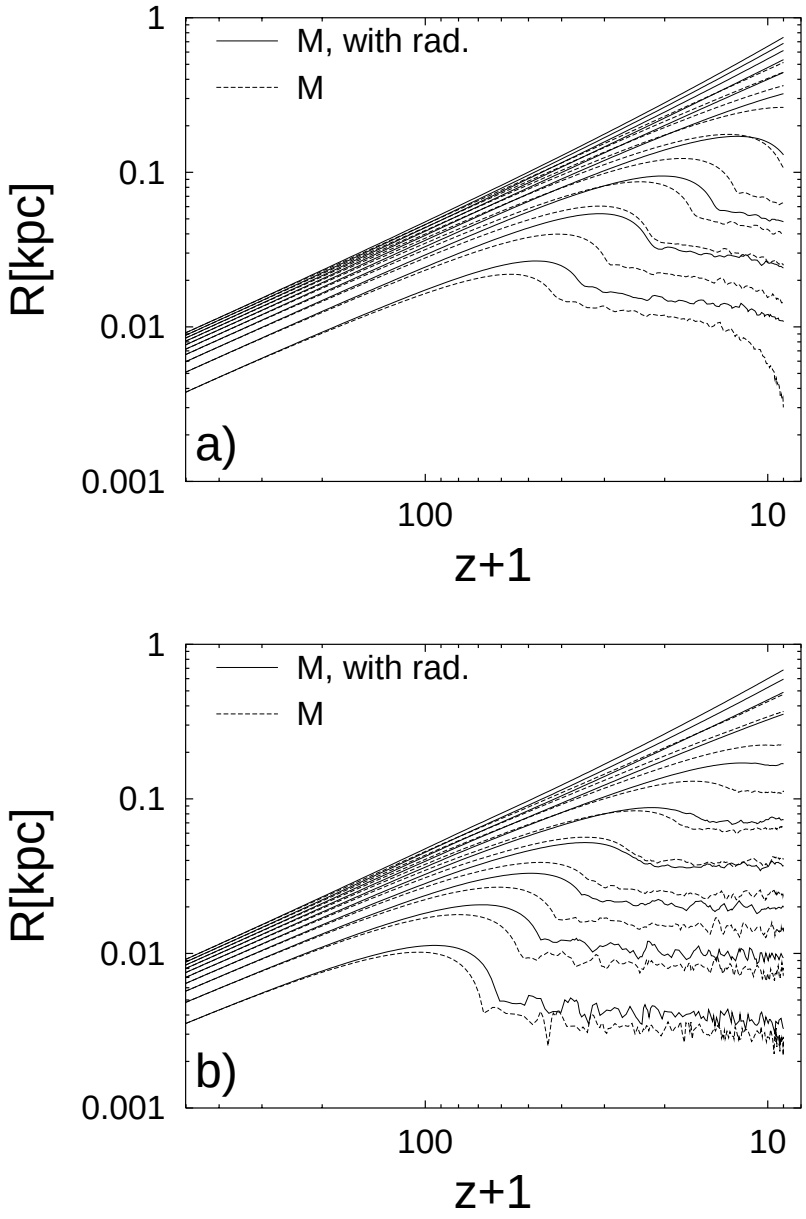


Fig. 3. Shell radii as functions of redshift. Solid curves are for the case when the radiation contribution is included. Dotted curves are the same as in Fig. 1a. Plots a and b correspond to baryon matter and dark matter, respectively.

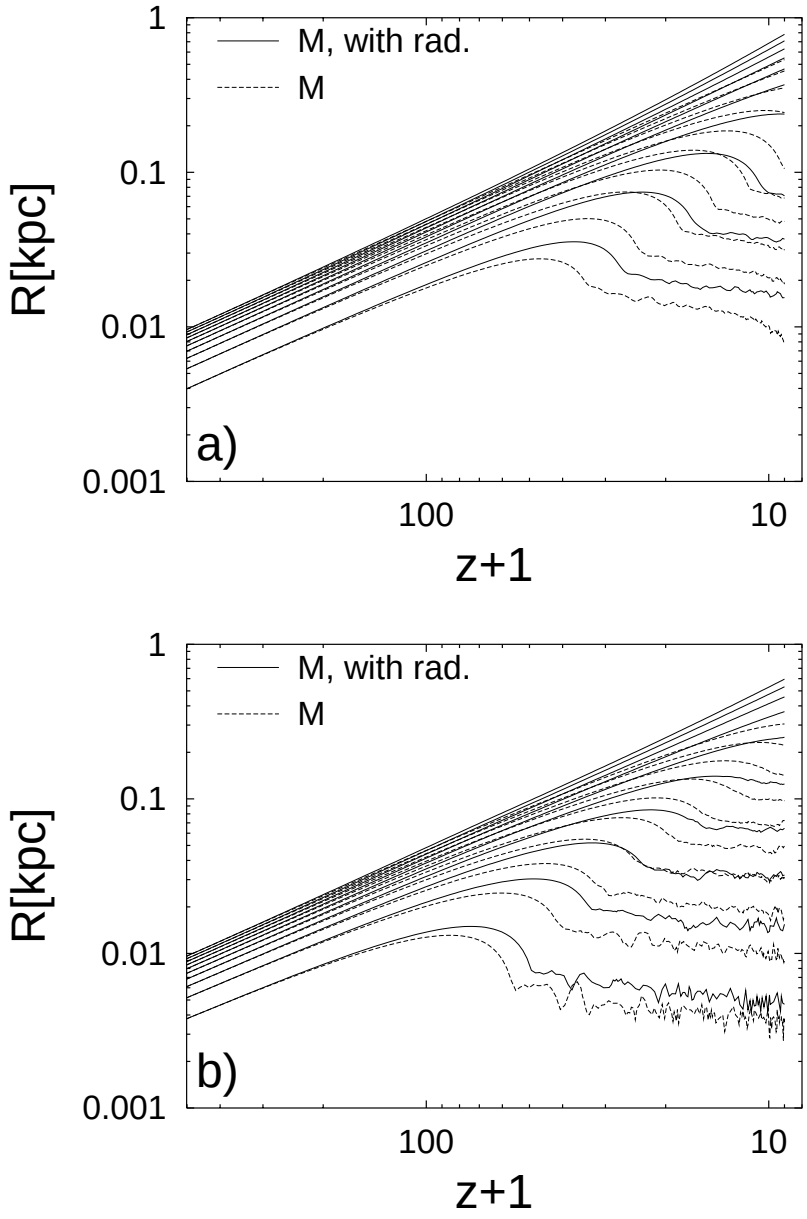


Fig. 4. The same as in Fig. 3 for the Gaussian form of the initial density perturbation.

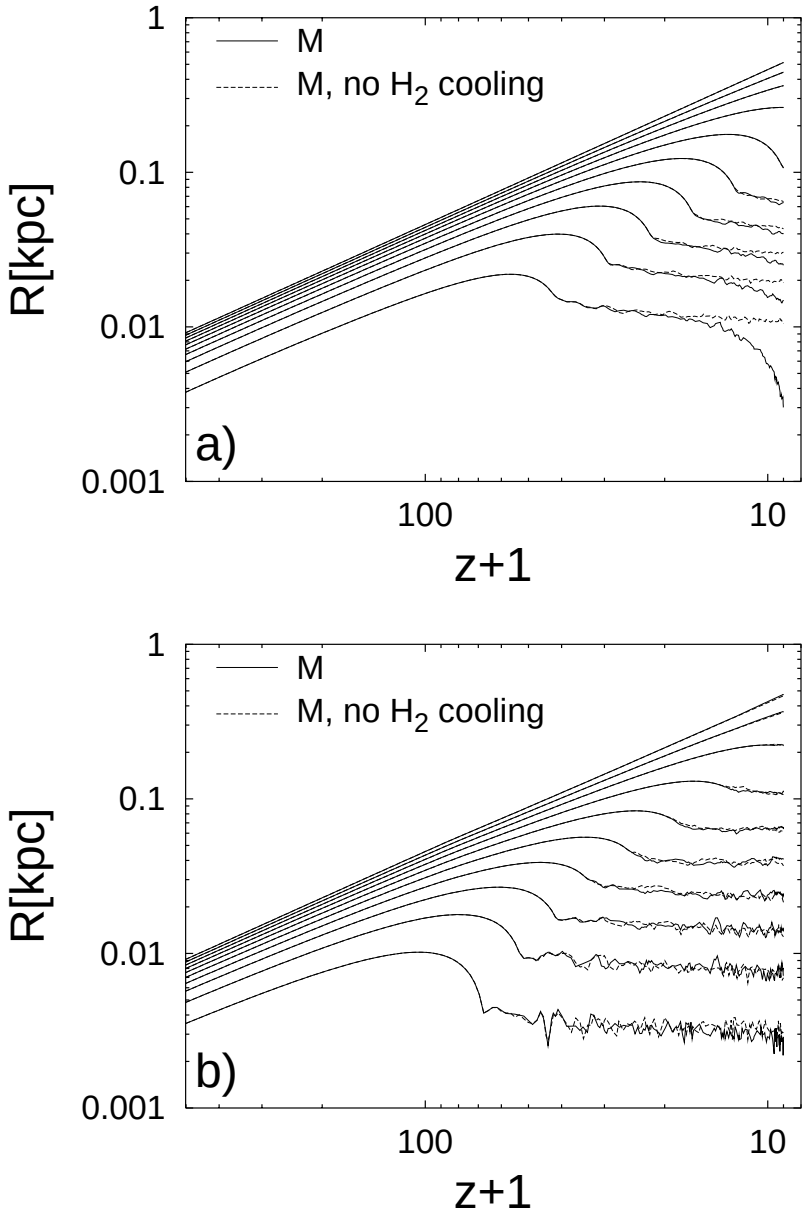


Fig. 5. Shell radii as functions of redshift with $H_2$ cooling (solid curves) and with no $H_2$ cooling (dashed curves). Plots a and b are for baryon matter and dark matter, respectively.

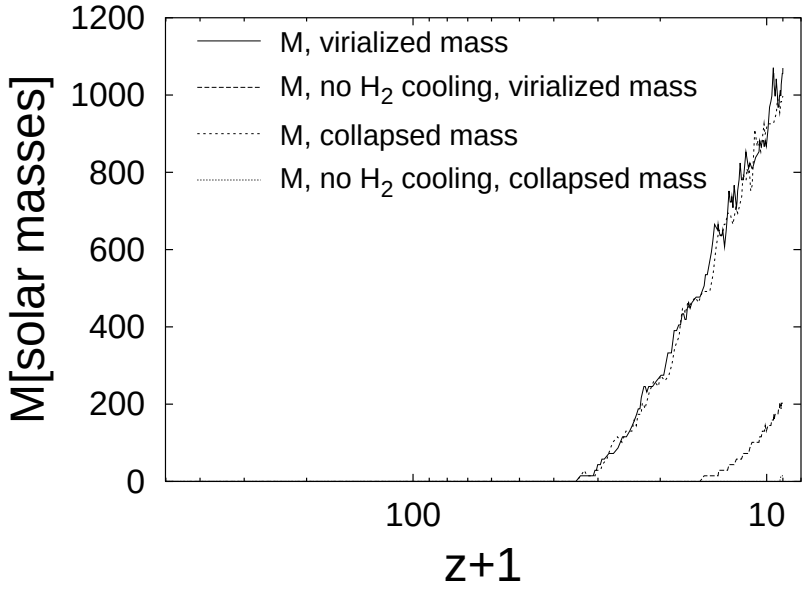


Fig. 6. The collapsed mass and the virialized mass as functions of redshift with $H_2$ cooling and with no $H_2$ cooling.

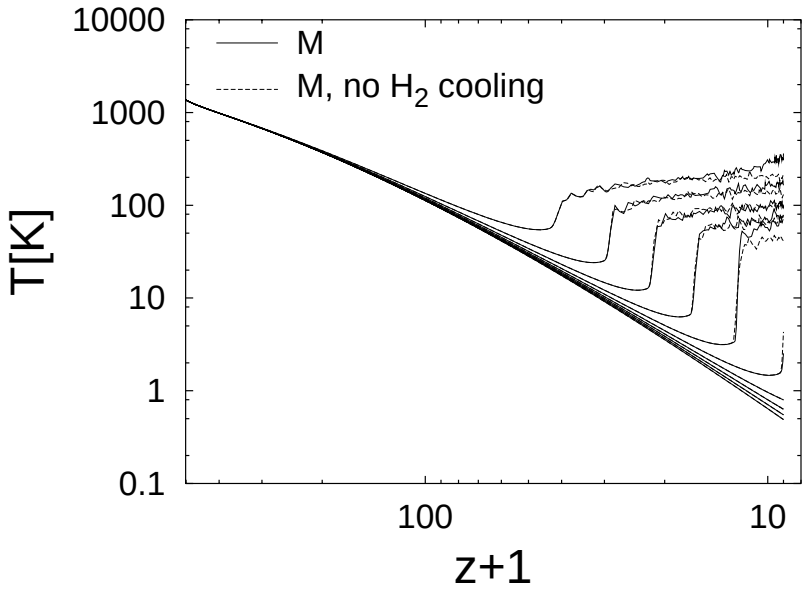


Fig. 7. The temperature of shells as a function of redshift. We show the temperature evolution with $H_2$ cooling and with no $H_2$ cooling.

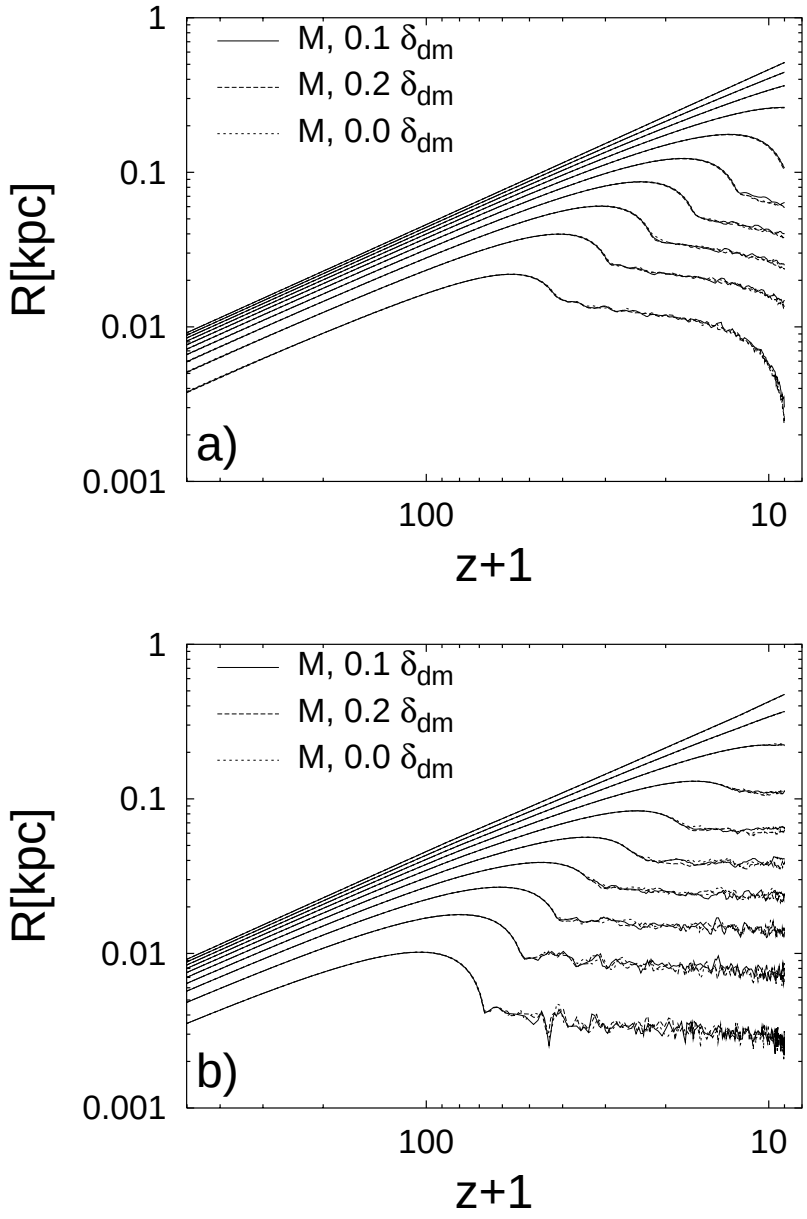


Fig. 8. The evolution of shell radii with redshift for different values of initial baryonic overdensities. Plots a and b correspond, respectively, to baryon matter and dark matter.

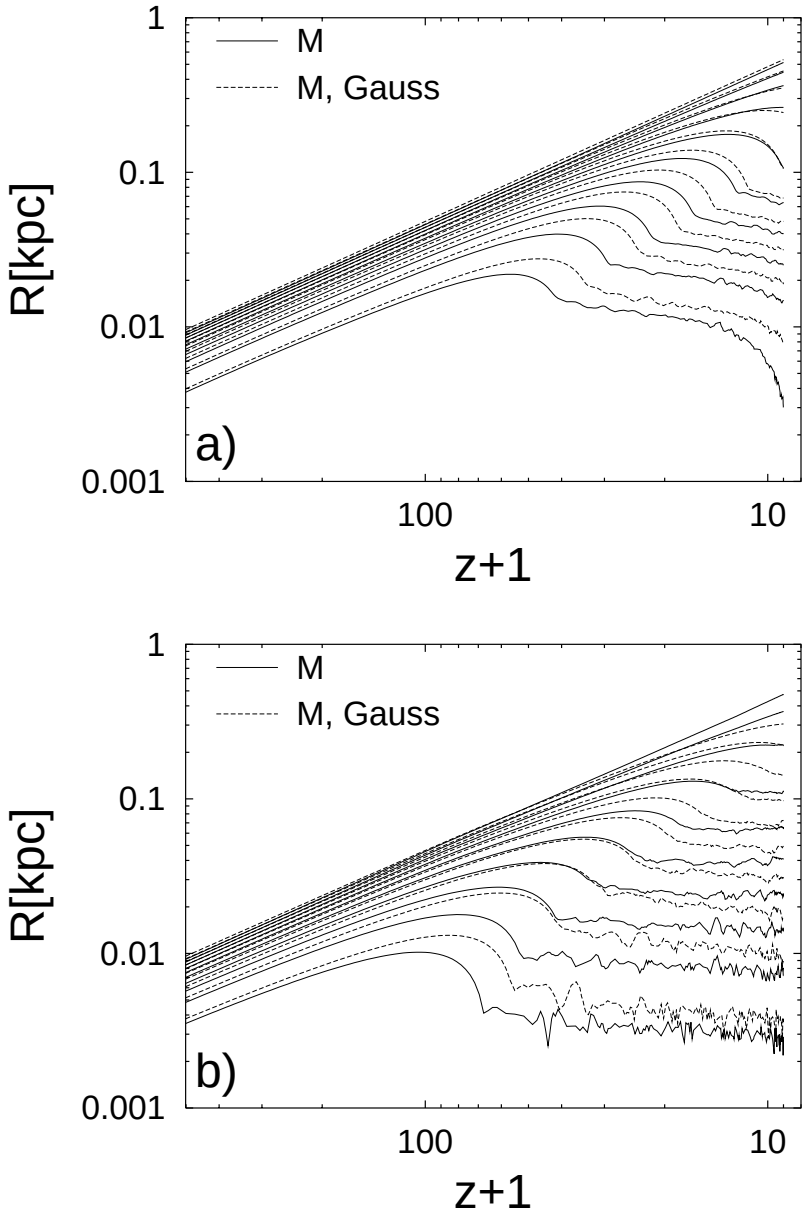


Fig. 9. Shell radii as functions of redshift for the sinusoidal (solid curves) and Gaussian (dashed curves) form of initial density perturbations. Plots a and b are for baryon matter and dark matter, respectively.

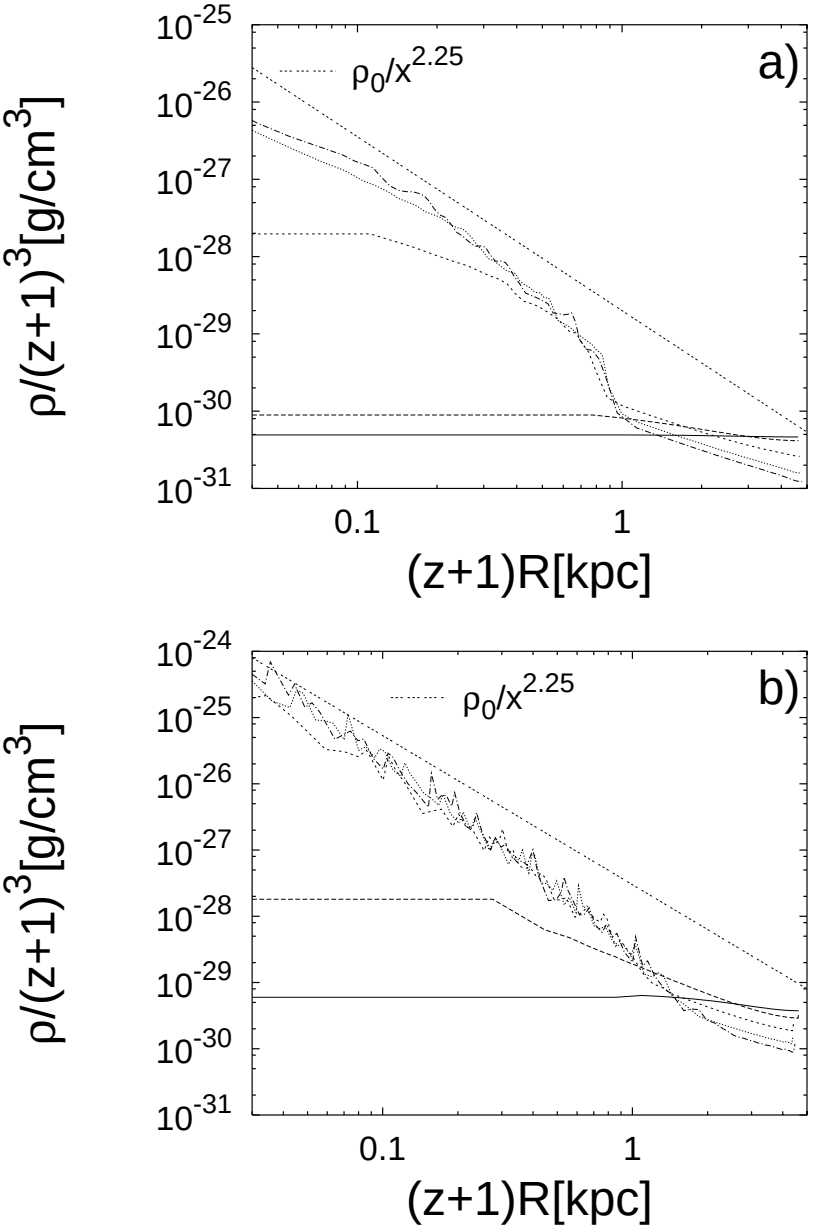


Fig. 10. Density profiles of baryon matter (plot a) and dark matter (plot b) for a few values of redshift.

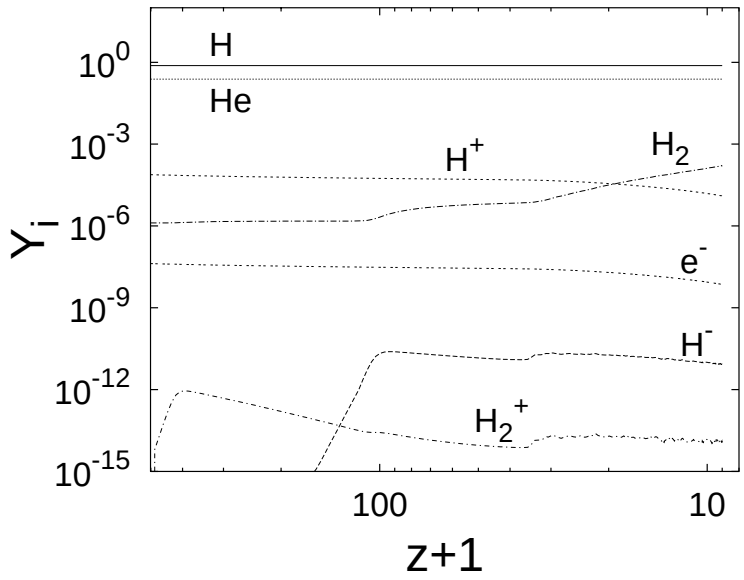


Fig. 11. Abundances of species as functions of redshift for a shell containing 12% of the bound mass.